ARTICLE OPEN

Check for updates

mGluR5 binding changes during a mismatch negativity task in a multimodal protocol with [^{11}C]ABP688 PET/MR-EEG

Cláudia Régio Brambilla[1,2✉], Tanja Veselinović[2], Ravichandran Rajkumar[1,2,3], Jörg Mauler[1], Andreas Matusch[4], Andrej Ruch[2], Linda Orth[2], Shukti Ramkiran[1,2], Hasan Sbaihat[1,2], Nicolas Kaulen[2], Nibal Yahya Khudeish[1], Christine Wyss[5], Karsten Heekeren[6,12], Wolfram Kawohl[5,7], Elena Rota Kops[1], Lutz Tellmann[1], Jürgen Scheins[1], Frank Boers[1], Bernd Neumaier[8], Johannes Ermert[8], Markus Lang[8], Stefan Stüsgen[8], Hans Herzog[1], Karl-Josef Langen[1,3,9], N. Jon Shah[1,3,10,11], Christoph W. Lerche[1,13,14] and Irene Neuner[1,2,3,13,14]

© The Author(s) 2021

Currently, the metabotropic glutamate receptor 5 (mGluR5) is the subject of several lines of research in the context of neurology and is of high interest as a target for positron-emission tomography (PET). Here, we assessed the feasibility of using [^{11}C]ABP688, a specific antagonist radiotracer for an allosteric site on the mGluR5, to evaluate changes in glutamatergic neurotransmission through a mismatch-negativity (MMN) task as a part of a simultaneous and synchronized multimodal PET/MR-EEG study. We analyzed the effect of MMN by comparing the changes in nondisplaceable binding potential (BP_{ND}) prior to (baseline) and during the task in 17 healthy subjects by applying a bolus/infusion protocol. Anatomical and functional regions were analyzed. A small change in BP_{ND} was observed in anatomical regions (posterior cingulate cortex and thalamus) and in a functional network (precuneus) after the start of the task. The effect size was quantified using Kendall's W value and was 0.3. The motor cortex was used as a control region for the task and did not show any significant BP_{ND} changes. There was a significant ΔBP_{ND} between acquisition conditions. On average, the reductions in binding across the regions were - 8.6 ± 3.2% in anatomical and - 6.4 ± 0.5% in the functional network ($p \leq 0.001$). Correlations between ΔBP_{ND} and EEG latency for both anatomical ($p = 0.008$) and functional ($p = 0.022$) regions were found. Exploratory analyses suggest that the MMN task played a role in the glutamatergic neurotransmission, and mGluR5 may be indirectly modulated by these changes.

Translational Psychiatry (2022)12:6 ; https://doi.org/10.1038/s41398-021-01763-3

INTRODUCTION

Glutamate is generally acknowledged as the most important excitatory neurotransmitter for normal brain function. Nearly all excitatory neurons and over half of all brain synapses in the central nervous system are glutamatergic [1]. Furthermore, an increasing number of studies have confirmed abnormal glutamatergic neurotransmission in several mental disorders such as schizophrenia, depression, mood disorders, sleep deprivation, and addiction [2–6]. As a result, interventions aimed at targeting the glutamate system are currently under development [7]. Prior to 2006, it was not possible to measure fluctuations in endogenous glutamate in vivo due to the lack of radiotracers for assessing the sensitivity of glutamate receptors to changed glutamate levels induced by a drug or stimuli tasks [8]. However, more recently, the use of 3-(6-methyl-pyridin-2-ylethynyl)-cyclohex-2-enone-O-[^{11}C] methyloxime, [^{11}C]ABP688 [9], and similar radiotracers have proved to be highly selective antagonistic PET agents for mGluR5. DeLorenzo and colleagues found a significant reduction in the nondisplaceable binding potential (BP_{ND}) of [^{11}C]ABP688 in ten healthy nonsmokers after the administration of ketamine [10]. Based on their findings, they hypothesized that the displacement of [^{11}C]ABP688 may occur as a result of indirect competition and/or receptor internalization.

Similarly, Esterlis and colleagues reported a significant reduction in mGluR5 availability in patients with a major depressive disorder and healthy controls following the administration of ketamine [11]. Furthermore, the superiority of [^{11}C]ABP688 in drug-challenge paradigms designed to probe glutamate transmission when compared with [^{18}F]FPEB was proven [12]. Thus, [^{11}C] ABP688 has emerged as a useful radiotracer and has expanded

[1]Institute of Neuroscience and Medicine, INM-4, Forschungszentrum Jülich GmbH, Jülich, Germany. [2]Department of Psychiatry, Psychotherapy and Psychosomatics, RWTH Aachen University, Aachen, Germany. [3]JARA – BRAIN – Translational Medicine, Aachen, Germany. [4]Institute of Neuroscience and Medicine, INM-2, Forschungszentrum Jülich GmbH, Jülich, Germany. [5]Department of Psychiatry, Psychotherapy and Psychosomatics, University Hospital of Psychiatry, Zurich, Switzerland. [6]Department of Psychiatry and Psychotherapy I, LVR-Hospital, Cologne, Germany. [7]Clienia Schlössli AG, Oetwil am See, Zurich, Switzerland. [8]Institute of Neuroscience and Medicine, INM-5, Forschungszentrum Jülich GmbH, Jülich, Germany. [9]Department of Nuclear Medicine, RWTH Aachen University, Aachen, Germany. [10]Institute of Neuroscience and Medicine, INM-11, Forschungszentrum Jülich GmbH, Jülich, Germany. [11]Department of Neurology, RWTH Aachen University, Aachen, Germany. [12]Present address: Department of Psychiatry, Psychotherapy and Psychosomatics, University Hospital of Psychiatry, Zurich, Switzerland. [13]These authors contributed equally: Christoph W. Lerche, Irene Neuner. [14]These authors jointly supervised this work: Christoph W. Lerche, Irene Neuner. ✉email: c.regio.brambilla@fz-juelich.de

Received: 12 July 2021 Revised: 22 November 2021 Accepted: 30 November 2021
Published online: 10 January 2022

the possibilities for in-depth research into the role of glutamatergic neurotransmission in both psychiatric disorders and healthy processes considerably.

One of the most commonly used and informative biological indicators of glutamatergic neurotransmission is the mismatch-negativity (MMN) paradigm [13]. MMN is an event-related potential (ERP) component, elicited by violations of a standard, that reflects the brain's ability to perform comparisons between repetitive stimuli, thereby providing an electrophysiological index linked to sensory learning and perception [14, 15]. This electrophysiological response can be detected using electroencephalography (EEG) or magnetoencephalography (MEG). The MMN is elicited by sudden changes in stimulation and shows the strongest intensity in temporo-frontal areas of the EEG maps [16]. Studies examining MMN have been performed in many clinical applications, especially in schizophrenia, and for better comprehension of auditory perception and sensory memory representations [17–19]. Thereby, most of the studies have found significant reductions in the MMN amplitude and longer latency times in patients with schizophrenia compared with healthy volunteers. Moreover, there is robust evidence indicating that this is mainly due to a dysfunction in N-methyl-D-aspartate (NMDA) receptors and is linked to impaired cognitive performance [19–21]. Further, significant reductions in the MMN amplitude were also observed following the administration of ketamine, which acts as an antagonist of NMDA [22–25]. As mGluR5 and NMDA are functionally correlated, measuring the availability of mGluR5 may also provide valuable information about NMDA receptors.

Given the close correlation between MMN and glutamatergic neurotransmission, a better understanding of the dynamics in this interaction is of high scientific interest. However, until now, these kinds of investigations were hardly possible due to technological limitations. The development of the simultaneous trimodal neuroimaging approach with positron-emission tomography (PET), magnetic resonance imaging (MR), and EEG (PET/MR-EEG) has accelerated research in this field in recent years. The main advantage of this approach is that structural and functional (via fMRI) and metabolic (via PET) data can be acquired simultaneously under the same physiological and psychological conditions [26].

In this work, we investigated the feasibility of simultaneous PET/MRI–EEG acquisition using [^{11}C]ABP688 to assess changes in glutamatergic neurotransmission through an MMN task. In order to determine any MMN effects in subjects during the PET measurement, we compared the changes in the BP_{ND} of [^{11}C]ABP688 between the pretask resting-state moments and MMN-task moments.

MATERIALS AND METHODS

Radiochemistry

Radiosynthesis of [^{11}C]ABP688 was performed according to [27]. The average molar activity at the injection time was 101.70 ± 45.33 MBq/nmol.

Subjects

Seventeen healthy, male, nonsmoker [8], and smoker [9] volunteers with a mean age of 38.47 ± 11.38 years were scanned in a single, multimodal session using a 3 T hybrid MR-BrainPET insert system (Siemens, Germany) [28] equipped with a 64-channel MR-compatible EEG system (Brain Products, Germany). The study was approved by the Ethics Committee of the Medical Faculty of the RWTH Aachen University and the German Federal Office for Radiation Protection. All subjects were scanned once, with an injected activity not exceeding 600 MBq. The MINI International Neuropsychiatric Interview was used to confirm that none of the subjects had a history of psychiatric disorders. Verbal and written informed consent were obtained from each volunteer according to the Declaration of Helsinki.

Multimodal acquisition

PET and bolus-infusion protocol. Our protocol was optimized and updated based on a previous publication [29]. Two syringes containing the radiotracer solution for the bolus and for the infusion were prepared 10 min prior to the bolus injection. The bolus injection (50% of total activity), followed by 65 min of infusion (activity in 100 ml of NaCl[1]; infusion pump at 92 ml/h rate), was administered after positioning the subject in the scanner. The average injected activity per subject was 468.50 ± 66.03 MBq. A distribution equilibrium was observed 30 min after the bolus injection [30, 31]. Starting simultaneously with the bolus injection, the PET data were acquired in list mode for 65 min.

Venous blood samples were taken at 2, 5, 10, 15, 20, 25, 30, 35, 40, 45, 50, 55, and 60 min after the bolus injection. Blood samples were centrifuged, and the plasma-activity concentration was measured in a gamma counter (Wallac 1480 Wizard). Furthermore, for the correction of tracer metabolization, the parent compound was separated from the metabolites in each sample by a solid-phase extraction using cartridges (Waters Sep-Pak® tC18).

MMN paradigm. The MMN paradigm consisted of changes in tone duration (standard = 50 ms, deviant = 100 ms). Auditory stimuli (1 kHz, 10 ms attack/decay) were presented in alternating sequences of mostly 50 ms with fewer 100 ms in positions 9 up to 16 after the standard tone (stimulus-onset asynchrony of 0.85 ± 0.05 s). The deviant positions were pseudo-randomized (only two equal positions following each other). A total of 1410 trials (8% deviant, 92% standard) were presented [32]. The subjects were instructed not to pay attention to the tones, and a silent video was presented to them for distraction.

EEG. Signals were recorded simultaneously with fMRI and PET during the MMN-task paradigm using a 64-channel MR-compatible EEG system. The EEG cap (BrainCap MR, EasyCap) consisted of 63 scalp electrodes, positioned according to the 10% system, covering the 10/20 area. One additional electrode was used for recording the electrocardiogram (ECG). Prior to recording, electrolyte gel (ABRALYT 2000, EASYCAP) was applied to each subject's head to increase the conductivity between scalp and EEG electrodes, followed by the placement of the EEG cap. The impedance of all recording electrodes was below 10 kΩ. The EEG data were recorded with a Brain Vision Recorder (Brain Products). The sampling rate of the EEG recording was 5 kHz. In order to avoid vibration effects, the helium pump of the MRI system was switched off during EEG recording.

MRI. Anatomical images were acquired with the magnetization-prepared rapid gradient-echo (MPRAGE) sequence (TR = 2250 ms, TE = 3.03 ms, 176 sagittal slices, 1 mm slice thickness, GRAPPA factor 2) after the tracer bolus injection. To provide functional images, a T_2^*-weighted echo-planar imaging (EPI) sequence (TR = 2.2 s, TE = 30 ms, FOV = 200 mm, slice thickness of 3 mm) was acquired when the tracer reached equilibrium. Single-voxel spectra were measured using a standard point-resolved spectroscopy (PRESS) sequence (after MPRAGE and before EPI acquisitions).

The EEG, MMN paradigm, and the fMRI were all synchronized to the PET acquisition. The first resting state (RS_1) started 30 min after the bolus injection (tracer equilibrium), followed by the MMN task and the second resting-state acquisition (RS_2). An MPRAGE image was used as an anatomical reference and for PET-attenuation correction [33]. Figure 1 shows the multimodal protocol in a schematic way.

PET image reconstruction and processing

As shown in Fig. 2(a), the image reconstruction was performed using 3D-OP-OSEM (2 subsets, 32 iterations), with an isotropic voxel of 1.25 mm, 153 slices, 256 × 256 voxels. A framing scheme was used to reduce reconstruction bias and the BP_{ND} errors were kept constant in the relevant acquisition interval [34]. Based on this scheme, PET true counts per frame based on this scheme were matched between subjects and synchronized with the different acquisition moments: pretask resting state and the MMN-task according to Fig. 2(c). For the subject with the lowest average of true counts, a total of 9.35×10^6 counts were registered in the last 5 min of the acquisition (see Fig. 2(b)), which corresponded with the third MMN-task interval. This value was taken as the fixed reference count per frame, and the three task-interval time fractions from the subject where this low

[1](NaCl = 0.9% sodium chloride solution).

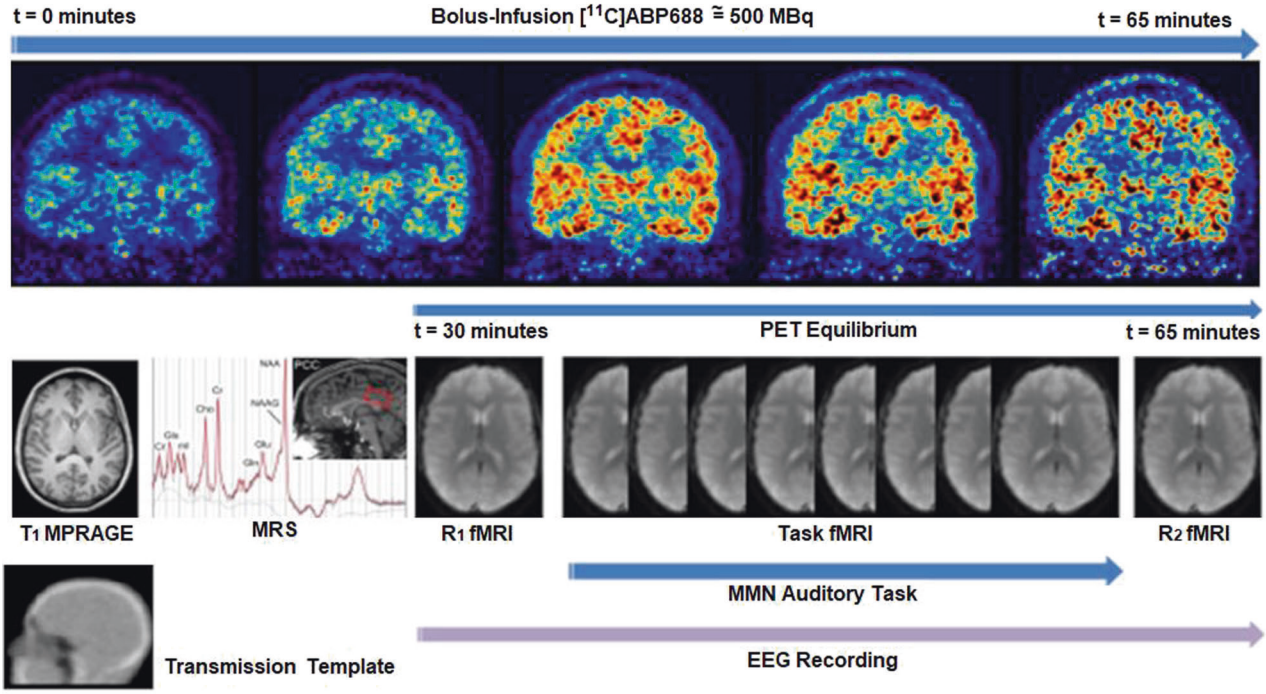

Fig. 1 Design of a measurement session. Schematic representation of the multimodal imaging approach.

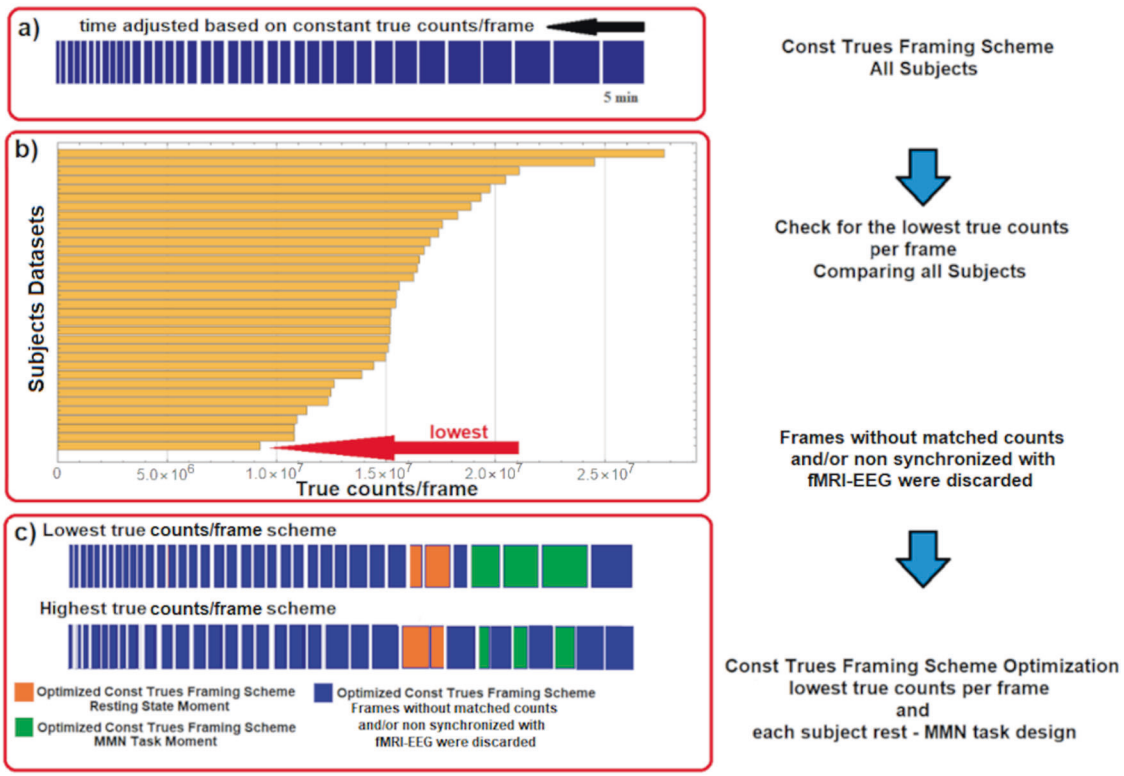

Fig. 2 PET-matched framing scheme applied in this [^{11}C]ABP688 study. a General frame scheme with variable time-frame lengths, enabling constant true counts/frame. **b** Comparison of all subjects to find the lowest-average true counts per frame. **c** Two individual Const Trues framing schemes showing the optimization to match the lowest-average true counts per frame between subjects and synchronized with the different acquisition moments: pretask resting state and the MMN task.

limit occurred were computed to give 0.267, 0.324, and 0.408 for the entire task interval. The task intervals were computed for each subject according to the total length of the MMN-task interval and these fractions. The three frames within the task time interval were then grown symmetrically around the center of these three intervals until the reference count (9.35×10^6) was reached, see Fig. 2(c). Frames without matched counts and/or not synchronized with fMRI-EEG were discarded. In this way, all seventeen subjects had the same number of counts during the RS_1 moments, and the reconstruction bias was equal for all [34]. In addition, the three frames representing the MMN-task moments were aligned at the

same time during the task for all subjects. The images were corrected for attenuation, random and scattered coincidences, and dead time. Post-processing with a 2.5 mm 3D Gaussian filter was applied. In addition, head motion correction based on the multiple-acquisition-frame (MAF) reconstruction scheme [35] was performed [36, 37].

Metabolite correction and plasma analysis

Aliquots of 400 µL plasma were diluted to 2.7 mL in water, loaded onto an injection loop, and passed through the SPE cartridge. This was followed by 5 mL of water using a motor syringe (7.7 mL over 2 min). Both the 2 ml aliquot of the eluate (totaling 7.7 mL and containing the metabolites) and the cartridge (containing the parent compound) were measured using a gamma borehole counter (ISOMED 2400) for a period of 60 s each. All activity concentrations were decay corrected according to the bolus-injection time. Biexponential curves were fitted to the fraction of the parent compound and to the total plasma-activity concentration. The corrected plasma activity curve was computed as the product of the total fitted plasma and the fitted fraction of the parent compound in the extract.

Equilibrium quality analysis

The [^{11}C]ABP688 parent compound time-activity curves (TACs) were normalized to their average values from 30 to 60 min, and the corresponding normalized radioactivity ranges were evaluated according to Eq. 1.

$$\text{Normalized Range}[\%]\left[\frac{(\max-\min)}{(\max+\min)}\right]\times 100. \quad (1)$$

The distribution volume (V_T) of [^{11}C]ABP688 was calculated (Eq. 2) for two anatomical reference and control regions (cerebellum gray matter and motor cortex) where both the tissue TAC and the metabolite-corrected plasma curve were flat. This indicates an equilibrium at the respective time points.

$$V_T[\mathrm{ml/cm^3}]=\frac{C_T}{C_P} \quad (2)$$

C_T denotes the [^{11}C]ABP688 concentration in the brain tissue, and C_P represents the unmetabolized [^{11}C]ABP688 parent compound in the plasma. The profiles were accepted as being flat if the normalized-range values from 30 to 60 min varied by no more than 10%. The TACs in this interval and from both regions were also adjusted using a linear regression in the average group curve, and the slopes were evaluated with reference to the equilibrium stability. Both regions were required to have a slope that was not significantly different from zero when a 95% confidence interval in the linear-regression analysis was considered.

PET quantitative data analysis

PNEURO/PMOD software v.3.9 was used to define the volumes of interest (VOIs) with T1 MPRAGE images serving as an anatomical reference. All images were processed in the PET subject's space, and the Hammers atlas [38] was applied for activity-concentration analysis. All VOIs in the gray matter cortex (GM) were defined with the maximum-probability operation. Furthermore, functional masks [39] were applied following conversion to the PET space. Finally, anatomical VOIs, comprising the whole brain, frontal left, frontal right, medial orbitofrontal cortex (mOFC), parietal left, parietal right, temporal left, temporal right, medial temporal, primary auditory, anterior cingulate cortex (ACC), posterior cingulate cortex (PCC), caudate, putamen, thalamus, motor cortex, and cerebellum GM, as well as functional VOIs, comprising the default-mode network (DMN), auditory network (AN), primary visual network (pVN), high visual network (hVN), visuospatial network (VN), language network (LN), salience network (SN), basal ganglia network (BgN), precuneus network (PN), and left and right executive control networks (LECN and RECN), were applied to extract the corresponding activity concentrations. To extract the activity concentrations from GM regions, only voxels with more than 50% probability of belonging to GM were considered. In previous studies, the cerebellum GM has been chosen as the most appropriate reference region for human-brain studies on mGluR5 [2, 3, 40, 41]. In all cases, the nondisplaceable binding potential (BP_{ND}) of [^{11}C]ABP688 was estimated as follows (Eq. 3):

$$\left[\left(\frac{C_T}{C_{\text{Cerebellum}}}\right)-1\right] \quad (3)$$

where C_T is the total radioligand concentration in the region of interest and $C_{\text{Cerebellum}}$ is the radioligand concentration in the cerebellar GM-reference tissue assumed to be nondisplaceable.

According to the aforementioned framing-scheme definition, the BP_{ND} was estimated for each of the acquisition moments: RS_1, MMN_1, MMN_2, and MMN_3. It was defined in this way to enable comparisons between RS_1 and each of the MMN moments, thus allowing the detection of the part of the MMN interval that has a significant effect when compared with the RS_1 baseline. The motor cortex was taken as a task-reference region for the analysis because, due to the nature of the MMN elicitation, it is not expected to be activated or show tracer displacements during the MMN task.

EEG processing

The EEG data were processed using the MATLAB-based (v.9.2, R2017a) software packages EEGLAB[2] v.13 [42]. The recorded raw EEG data were imported to EEGLAB and downsampled to 1024 Hz. The gradient artifacts that were mixed with the EEG signals linearly due to the switching of the magnetic gradients were removed using the FASTR tool [43]. The EEG data were again downsampled to 256 Hz and filtered between 1 and 20 Hz using a Hamming windowed sinc finite impulse-response filter. Bad channels were identified and removed using the EEGLAB function clean_rawdata. Artifact subspace reconstruction [44] was performed to remove the nonstationary artifacts, such as head movement. An adaptive optimal basis-set algorithm [45] was used to remove the ballistocardiogram artifacts in the EEG data caused by pulsatile blood flow. Ocular artifacts were removed by using an automatic blind-source separation algorithm [46]. EEG signals were re-referenced to an average reference. In order to remove further residual artifacts, independent component analysis [47] was performed, and the multiple artifact-rejection algorithm [48] was used to classify and remove artifactual components. The EEG signals were segmented between 200 ms prior to—and 400 ms after the standard and frequent auditory stimuli marker position. Baseline correction was performed using 100 ms data prior to the stimuli-marker. The segmented EEG data were averaged over trials. MMN latency was measured between 100 ms and 300 ms post deviant tone at the C_Z, P_Z, and F_Z EEG channels individually and at the average of the F_3, F_Z, F_4, C_3, C_Z, and C_4 channels.

Statistical analysis

Statistical analysis was performed using the Statistical Package v.25 (IBM SPSS Inc., Chicago, IL). Differences between acquisition conditions were compared using the nonparametric Wilcoxon Rank test (between baseline and each task moment separately). Additionally, baseline and task moments were evaluated in repeated measures using the Friedman test. Within-subject SE-bar standardization was performed according to [49]. Corrections for multiple comparisons using the Bonferroni method were applied in the evaluation for task effects in the within-subject design, and the updated significance was 0.001. The Kendall's W coefficient was used to evaluate the effect size. It tests the ΔBP_{ND} in each region and gives a value that ranges between 0 and 1. A Kendall's W interpretation of 0.2 represents a small effect, 0.5 a moderate effect, and above 0.8 a strong effect. The extent of BP_{ND} changes during the MMN (calculated as $[(BP_{ND_{MMN}}-BP_{ND_{Baseline}})/BP_{ND_{Baseline}}]*100$) in regions that showed significant binding changes) was examined for an existence of a significant Pearson's correlation with the EEG-latency times during the MMN task. Due to the purely exploratory approach, these correlations were not corrected for multiple testing.

This study describes the effect of the MMN paradigm on the BP_{ND}, and for regions that may show significant task effects, it also presents correlations between the binding changes and the EEG-latency times represented by the time range from the onset of stimuli until the MMN auditory stimulation peak.

[2](https://sccn.ucsd.edu/eeglab/index.php).

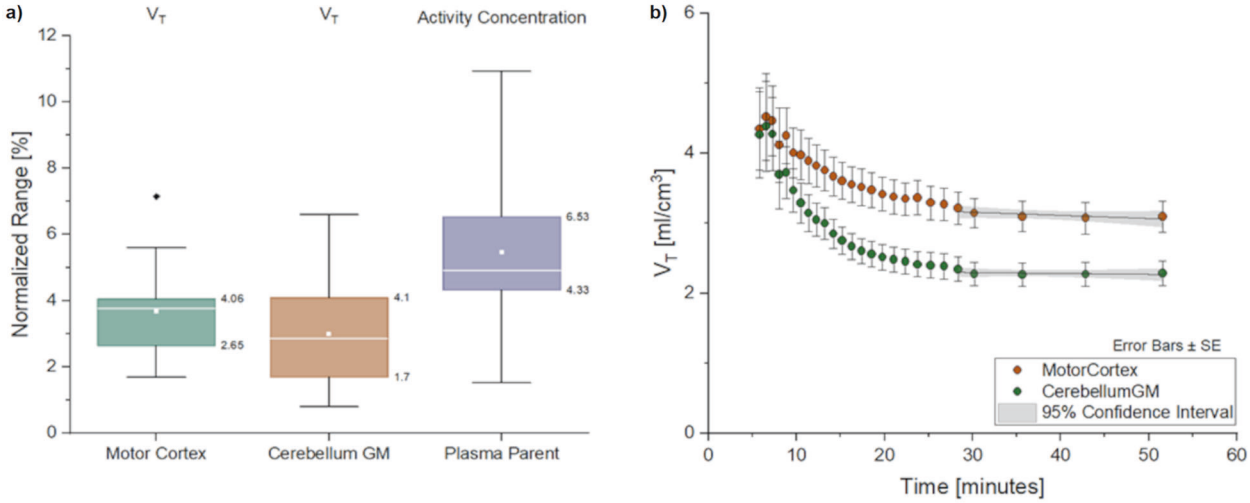

Fig. 3 Equilibrium quality evaluation/inspection represented by regional cerebral uptake of [C]ABP688 expressed as distribution volume referenced to plasma parent, V. a Normalized-range variations of the V_T values in the plateau range (30–60 min) for the motor cortex and cerebellum GM-control regions during the equilibrium phase. The plasma parent compound normalized activity-concentration range for evaluating the equilibrium quality is also shown. **b** Average V_T curves and the linear regression applied to the data plateau range (30–60 min) for the slope analysis. SE = standard error of the mean (mean/$\sqrt{n}$), where n = sample size.

RESULTS

Equilibrium Quality

Figure 3a shows the percentual normalized range values of the V_T for the two anatomical reference and control regions, the cerebellum GM and the motor cortex, and the blood plasma-activity concentration for all subjects. For all quantities measured, values were lower than 5%, except for variations of 5.46 ± 2.38% in the plasma values during the equilibrium phase.

Figure 3b shows the average V_T vs. time curves for both the reference and task-control regions and the adjusted linear-regression line in the expected equilibrium interval. Both regions showed slope values that were not significantly different from zero based on a 5% significance level in the analysis.

Slope values in both the reference and control regions are given in Table 1. It can be noted that no significant differences in the slopes were found for either region. This means that the equilibrium was well established, and these regions can serve as reference and task-control regions.

Binding changes ΔBP_{ND} during the MMN task

The task effects were analyzed separately for anatomical and functional VOIs by estimating the BP_{ND} using the simple ratio method. The statistical comparisons were performed using nonparametric Wilcoxon and Friedman tests with $p \le 0.001$ (16 anatomical regions and 3 comparison pairs) and $p \le 0.002$ (11 functional regions and 3 comparison pairs) after Bonferroni correction. Kendall's W coefficient was used to measure the effect size for each region. Table 2 shows the results for anatomical regions, and Table 3 shows the results for functional regions. Note that the motor cortex is the control region for the task-effect analysis and should not show any effect.

The effect size due to the MMN task is classified as a small effect according to the Kendall's W coefficient scale. This is also true when compared with the effect sizes caused by pharmacological challenges obtained, e.g., with ketamine and [^{11}C]ABP688. These challenges showed effects of 0.88, as represented by a similar scale [50]. The ketamine effects are considered high and are in agreement with the high surge of glutamate release in the brain, as identified in a PET-depression study [11].

Figure 4a shows the BP_{ND} curves for the anatomical and functional regions with significant differences in binding during the MMN task when compared with the motor cortex. Figure 4b shows parametric images (sagittal plane with lateral and medial) of the average BP_{ND} for the different acquisition moments.

It is possible to identify a slight reduction in the BP_{ND} values during the transition between MMN_2 and MMN_3. These changes are hardly observable with the naked eye. However, they can be noted by comparing the BP_{ND} curves (Fig. 4a), proving that the values decrease (−6.39 ± 2.49% PCC, [3] −10.87 ± 6.34% thalamus and −6.7 ± 3.10% PN) slightly over time. Also, the Kendall's W scale showed that the MMN task had a low effect over time, which explains the very tiny change between the acquisition moments.

Table 1. Slope values and SE in control regions.

Regions	Value	Standard error	t-Value	Prob > $\left\|\frac{\alpha}{2}\right\|$
motor cortex	−0.004	0.002	−1.962	0.144
cerebellum GM	−0.001	0.001	−0.751	0.506

Correlation between ΔBP_{ND} and EEG-latency times during the MMN task

For the three regions that showed binding changes, the PCC and PN showed correlations with the EEG P_z electrode-latency times of $r = -0.549$; $p = 0.023$, and $r = -0.552$; $p = 0.022$, with a significance of $p < 0.05$. In the thalamus, the correlation between the extent of the BP_{ND} change during the MMN and the average of latencies for three central (C_3, C_4, and C_z) and three frontal (F_3, F_4 and F_z) electrodes was $r = 0.623$, $p = 0.008$, with a significance of $p < 0.01$. Figure 5 shows the auditory-evoked potential during the task as an average of the EEG channels and the MMN wave.

DISCUSSION

This in vivo imaging study used simultaneous PET/MR-EEG imaging in a group of healthy male subjects with the aim of revealing the first evidence for MMN task-induced changes in glutamatergic neurotransmission. After corrections for multiple comparisons using the Bonferroni method, we observed a significant decrease in the availability of mGluR5 in the thalamus,

[3](PCC showed significant result in the Wilcoxon test, but not in Friedman test).

Table 2. Task effect results for anatomical brain regions analyzed with the Wilcoxon and Friedman tests and corrected using the Bonferroni method.

Brain region	*p* value – Wilcoxon RS_1 x MMN_1/ MMN_2/MMN_3	*p* value – Friedman RS_1 x MMN_1/ MMN_2/MMN_3	Effect's size Kendall's W	Acquisition moment occurrence
Whole brain GM	0.652/0.266/0.027	0.678	0.030	–
Frontal left	0.246/0.021/0.003	0.004	0.258	–
Frontal right	0.209/0.024/0.002	0.002	0.283	–
mOFC	0.435/0.619/0.102	0.630	0.034	–
Parietal left	0.148/0.027/0.005	0.007	0.236	–
Parietal right	0.209/0.075/0.006	0.083	0.131	–
Temporal left	0.356/0.193/0.055	0.487	0.048	–
Temporal right	0.462/0.136/0.013	0.208	0.089	–
Temporal Med	0.981/0.758/0.093	0.615	0.035	–
Primary auditory	0.553/0.209/0.061	0.678	0.030	–
ACC	0.162/0.013/0.011	0.010	0.222	–
PCC	0.035/0.024/0.001*	0.005	0.255*	MMN_3
Caudate	0.266/0.113/0.006	0.039	0.164	–
Putamen	0.522/0.286/0.227	0.796	0.020	–
Thalamus	0.017/0.227/0.001*	0.001*	0.347*	MMN_3
Motor cortex	0.227/0.245/0.193	0.615	0.035	–

Effect size was evaluated using Kendall's W.
*Significant effects ($p \leq 0.001$).

Table 3. Task effect results for functional brain regions analyzed with the Wilcoxon and Friedman tests and corrected using the Bonferroni method. Effect size was evaluated using Kendall's W.

Brain region	*p* value – Wilcoxon RS_1 x MMN_1/ MMN_2/MMN_3	*p* value – Friedman RS_1 x MMN_1/ MMN_2/MMN_3	Effect's size Kendall's W	Acquisition moment occurrence
DMN	0.162/0.027/0.005	0.029	0.203	–
AN	0.148/0.981/0.084	0.467	0.062	–
pVN	0.868/0.102/0.009	0.225	0.197	–
hVN	0.492/0.523/0.005	0.808	0.147	–
VN	0.061/0.044/0.004	0.090	0.153	–
LN	0.331/0.162/0.011	0.090	0.114	–
SN	0.522/0.055/0.006	0.090	0.181	–
BgN	0.831/0.687/0.019	0.225	0.106	–
PN	0.068/0.004/0.001*	0.0005*	0.307*	MMN_3
LECN	0.245/0.049/0.004	0.029	0.175	–
RECN	0.943/0.463/0.013	0.225	0.178	–
Motor cortex	0.209/0.246/0.193	0.467	0.042	–

*Significant effects ($p \leq 0.001$).

the PCC (except in Friedman analysis), and the PN during the MMN task. The effect size of the observed changes was small ($W = 0.3$) when compared with effect sizes as a result of pharmacological challenges with ketamine [10, 11], where effects of 0.88 could be demonstrated [50]. The authors attribute the decrease in mGluR5 availability to the rapid surge in extracellular glutamate leading to mGluR5 downregulation or internalization. The glutamate-surge hypothesis originates from rodent data showing that a single administration of ketamine rapidly induces increases in glutamate efflux [51] and cycling [52]. Accordingly, the change in mGluR5 binding observed in our study during the MMN task could be related to an increase in glutamate in the regions pointed out, although to a much smaller extent.

Separate temporal and frontal generators of MMN have been consistently identified using various source-localization methods [53]. A temporal generator for MMN is localized in the primary auditory cortex and is considered to be the primary generator responsible for MMN elicitation [54]. However, a recent study with nonhuman primates showed that the thalamic region is also involved in MMN [55]. The involvement of the auditory thalamus was previously found in healthy human participants [56], and numerous investigations suggest that the human thalamus serves as a global hub that is connected with the entire cortex, relaying sensory information to the cortex and mediating the transmission of cortico-cortical information [57]. Moreover, the thalamus could be indicated as being a critical integrative hub for functional brain networks engaged with multiple cognitive functions [58]. The auditory thalamus (medial geniculate body) represents the primary sensory input to auditory-cortex processing [59]. Thus, it is the information bottleneck for neural representations of sounds being sent to the auditory cortex and plays a critical role in the complex auditory processing [59], which forms an important part of the MMN. Correspondingly, our findings confirm thalamic involvement in the MMN and further relate this involvement to glutamatergic neurotransmission.

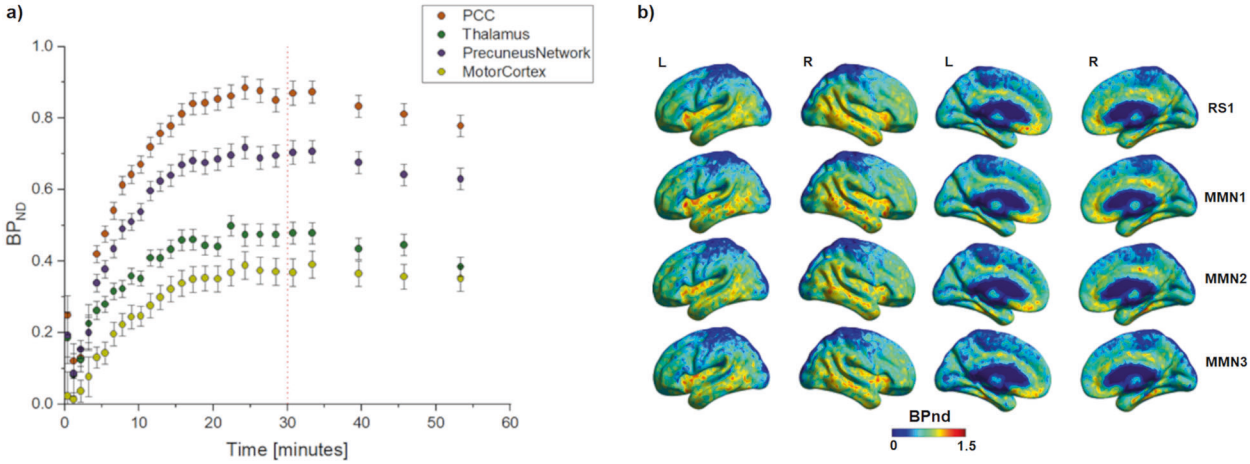

Fig. 4 Task effect results shown by the regional and voxel-wise cerebral uptake of [C]ABP688 expressed as distribution volume referenced to cerebellum grey matter, BP. a BP_{ND} curves for the anatomical and functional brain regions analyzed. Significant effects can be seen in the healthy group. The red line marks the start point of tracer equilibrium phase. After 30 min, the first two time points represent RS_1 and the remaining three time points represent the MMN task moments (MMN_1, MMN_2, and MMN_3). **b** BP_{ND} parametric images for the group average per acquisition moment.

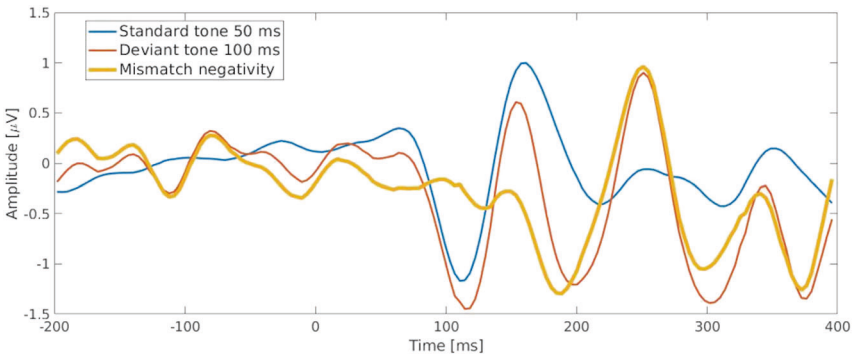

Fig. 5 Auditory-evoked potential (AEP) of standard and deviant tones during the MMN paradigm calculated by averaging F_3, F_Z, F_4, C_3, C_Z, and C_4 channels. Additionally, the mismatch-negativity difference wave obtained by subtracting the standard from deviant event-related potentials is also shown.

We observed a significant reduction in the binding potential for the PCC and PN, which is in accordance with previously reported involvement of these regions in the mismatch response [60].

The PCC is a highly anatomically connected part of the posteromedial cortex and represents a central part of the DMN [61]. Moreover, some evidence suggests that the PCC plays a more direct role in regulating the focus of attention [62]. Thus, the finding of a significant decrease in BP_{ND} in the PCC during the MMN task might be understood as an effect of a further shift in attention due to the tone alterations.

The PN is a network centered at the precuneus. It has recently been argued that it is functionally independent of the DMN, although this remains controversial due to the considerable extent of spatial adjacency and overlap [63]. However, the core region of the PN, the precuneus, is known to be widely connected with other regions in the brain [64, 65], and numerous studies have indicated its involvement in a wide range of cognitive processes [66]. Also, a strong structural and functional connectivity of the precuneus has been shown with the thalamus and the DMN [64]. Furthermore, previous investigations have demonstrated that the PN plays an important role in the detection of novelty [67]. Accordingly, the observed reduction in the binding in our study may be an expression of the glutamate surge in the PN in response to the tones heard during the MMN task.

Given that [^{11}C]ABP688 and glutamate bind at different sites on the receptor, this decrease cannot be due to direct competition, and the mechanism responsible for the changes in binding after an MMN challenge relating to mGluR5 is still not completely understood. After observing a significant ketamine-induced reduction in mGluR5 availability, Esterlis et al. hypothesized that binding changes may be due to increased mGluR5 internalization reducing affinity by altering the local intracellular milieu [11]. In our study, we demonstrated, for the first time, that this alteration may occur due to an MMN challenge. Accordingly, the exposure to a certain amount of endogenous glutamate released during the MMN task may have caused an internalization of the glutamatergic receptors. This, in turn, may have indirectly induced changes in the BP_{ND}. One conceivable course of events could be that the released endogenous glutamate binds to the main site of the mGluR5 receptors, promoting their internalization or simply a conformational rearrangement, and thus (minor) structural changes, which lead to a decrease in the affinity of [^{11}C]ABP688 for the receptor and therefore to a displacement into the allosteric site.

To date, the glutamatergic basis of MMN has been hypothesized through indirect reasoning from other studies [68, 69], and a direct glutamatergic readout has only been used in this context in a few cases. In their spectroscopic study, Stone and colleagues showed an association between smaller frontal MMN amplitudes and lower levels of the overlapping resonance of glutamate and glutamine in the thalamus in participants at risk of psychosis [70]. However, in their study, the recording of MMN and the

spectroscopy occurred at different points in time, while in our study, all data modalities were acquired simultaneously. This allows for a higher level of synchronization, and the change in the binding could be captured exactly during the MMN task.

The observation of the tiny effect of the MMN task on the mGluR5 binding was possible due to a previous study where the reconstruction bias was minimized and kept constant during the equilibrium plateau where BP_{ND} is estimated, thus enabling the detection of changes larger than the bias range of 2.56 ± 3.92% [34]. This was achieved by applying an optimized constant trues framing scheme. In addition, since within-subject SE standardization was also applied in the analysis, the chances of finding small changes also increased due to the reduction in concomitant variance [49].

Another interesting finding from our study, which was only possible due to the multimodal, simultaneous PET/MR and EEG data acquisition, was the significant correlation between the changes in mGluR5 availability due to the MMN task (namely in regions where we observed significant BP_{ND} changes) and EEG latencies captured with several electrodes.

Hereby, the most prominent association concerned the thalamus: the higher BP_{ND} change was associated with the longer average latency time captured with three central and three frontal electrodes. The thalamus has been referred to as the gateway (or hub) of nearly all sensory inputs (except for the olfactory system) to the corresponding cortical areas through direct thalamocortical circuits [71, 72]. Consequently, thalamic operations require highly complex inhibitory activity, mainly arising from the GABAergic mechanisms within the thalamic circuits [73]. As the GABA release is strongly mediated by the mGluR activation [74], the association between the higher [^{11}C]ABP688 displacement and the longer latencies might be an expression of the primary inhibitory effect of the glutamatergic surge in the thalamus.

In contrast, the greater extent of BP_{ND} changes in the PCC and PN during the MMN task was associated with shorter latencies. Considering the previous findings, where longer latencies were reported in several conditions with impaired cognitive performance (chronic schizophrenia [21], Alzheimer's disease [75], and mild cognitive impairment [76]), and the fact that the MMN can be considered an index of the context-dependent information processing at the level of the primary and secondary auditory cortices [77], our findings provide an indication for a link between higher glutamatergic activity in the PN and PCC and faster auditive information processing. As the generation of MMN is a fully automatic process and therefore independent of the subject's attention [78, 79], an extensive glutamatergic response to the stimulus violation in the PCC and the PN might have a decisive role for fast automatic information processing.

Despite the positive results obtained, it is important to consider that the study may be limited by the relatively small sample size and the combined analysis of smokers and nonsmokers. Consequently, additional studies are needed to understand the complex effects that the cognitive tasks involved in MMN auditory stimulation may have on the glutamatergic system when imaged with PET. Finally, although many corrections have been applied to minimize the bias caused by image reconstruction, quantification, and statistical analysis, a residual bias in the results cannot be completely excluded.

With the reported approach, our study provides evidence of a reduction in glutamatergic receptor binding and indirectly shows an active alteration in glutamatergic neurotransmission during auditory information processing in healthy subjects for the first time. In light of this, further replication is required, along with investigations into whether the extent of the changes recorded is related to cognitive abilities, or in the case of patients, whether there is a correlation with clinical symptomatology. Thus, our approach may be applied to further investigate the role of glutamatergic neurotransmission in healthy subjects and in patients with various mental disorders.

REFERENCES

1. Purves D, Augustine G, Fitzpatrick D, Katz L, LaMantia AS, McNamara JO, et al. Neuroscience. edition n, editor. Sunderland (MA): Sinauer Associates; 2001.
2. Akkus F, Treyer V, Ametamey SM, Johayem A, Buck A, Hasler G. Metabotropic glutamate receptor 5 neuroimaging in schizophrenia. Schizophr Res 2017;183:95–101.
3. Akkus F, Mihov Y, Treyer V, Ametamey SM, Johayem A, Senn S, et al. Metabotropic glutamate receptor 5 binding in male patients with alcohol use disorder. Transl Psychiatry 2018;8:17.
4. Sanacora G, Zarate CA, Krystal JH, Manji HK. Targeting the glutamatergic system to develop novel, improved therapeutics for mood disorders. Nat Rev Drug Discov 2008;7:426–37.
5. Milella MS, Marengo L, Larcher K, Fotros A, Dagher A, Rosa-Neto P, et al. Limbic system mGluR5 availability in cocaine dependent subjects: a high-resolution PET [11C]ABP688 study. Neuroimage 2014;98:195–202.
6. DeLorenzo C, Sovago J, Gardus J, Xu J, Yang J, Behrje R, et al. Characterization of brain mGluR5 binding in a pilot study of late-life major depressive disorder using positron emission tomography and [11C]ABP688. Transl Psychiatry 2015;5:e693.
7. Pillai RLI, Tipre DN. Metabotropic glutamate receptor 5 – a promising target in drug development and neuroimaging. Eur J Nucl Med Mol Imaging 2016;43:1151–70.
8. Miyake N, Skinbjerg M, Easwaramoorthy B, Kumar D, Girgis RR, Xu X, et al. Imaging changes in glutamate transmission in vivo with the metabotropic glutamate receptor 5 tracer [11C] ABP688 and N-acetylcysteine challenge. Biol Psychiatry 2011;69:822–4.
9. Ametamey SM, Kessler LJ, Honer M, Wyss MT, Buck A, Hintermann S, et al. Radiosynthesis and preclinical evaluation of 11C-ABP688 as a probe for imaging the metabotropic glutamate receptor subtype 5. J Nucl Med 2006;47:698–705.
10. DeLorenzo C, DellaGioia N, Bloch M, Sanacora G, Nabulsi N, Abdallah C, et al. In vivo ketamine-induced changes in [11C]ABP688 binding to metabotropic glutamate receptor subtype 5. Biol Psychiatry 2015;77:266–75.
11. Esterlis I, DellaGioia N, Pietrzak RH, Matuskey D, Nabulsi N, Abdallah CG, et al. Ketamine-induced reduction in mGluR5 availability is associated with an antidepressant response: an [11C]ABP688 and PET imaging study in depression. Mol Psychiatry 2018;23:824–32.
12. Holmes SE, Gallezot J-D, Davis MT, DellaGioia N, Matuskey D, Nabulsi N, et al. Measuring the effects of ketamine on mGluR5 using [18F]FPEB and PET. J Cereb Blood Flow Metab 2019;40:2254–64.
13. Nagai T, Kirihara K, Tada M, Koshiyama D, Koike S, Suga M, et al. Reduced mismatch negativity is associated with increased plasma level of glutamate in first-episode psychosis. Sci Rep. 2017;7:2258.
14. Naatanen R, Paavilainen P, Tiitinen H, Jiang D, Alho K. Attention and mismatch negativity. Psychophysiology 1993;30:436–50.
15. Garrido MI, Kilner JM, Stephan KE, Friston KJ. The mismatch negativity: a review of underlying mechanisms. Clin Neurophysiol 2009;120:453–63.
16. Sams M, Paavilainen P, Alho K, Naatanen R. Auditory frequency discrimination and event-related potentials. Electroencephalogr Clin Neurophysiol 1985;62:437–48.
17. van Zuijen TL, Sussman E, Winkler I, Naatanen R, Tervaniemi M. Auditory organization of sound sequences by a temporal or numerical regularity-a mismatch negativity study comparing musicians and non-musicians. Brain Res Cogn Brain Res 2005;23:270–6.
18. van Zuijen TL, Simoens VL, Paavilainen P, Naatanen R, Tervaniemi M. Implicit, intuitive, and explicit knowledge of abstract regularities in a sound sequence: an event-related brain potential study. J Cogn Neurosci 2006;18:1292–303.
19. Pekkonen E, Huotilainen M, Katila H, Karhu J, Naatanen R, Tiihonen J. Altered parallel auditory processing in schizophrenia patients. Schizophr Bull 1999;25:601–7.
20. Naatanen R, Kahkonen S. Central auditory dysfunction in schizophrenia as revealed by the mismatch negativity (MMN) and its magnetic equivalent MMNm: a review. Int J Neuropsychopharmacol 2009;12:125–35.
21. Domján N, Csifcsák G, Drótos G, Janka Z, Szendi I. Different patterns of auditory information processing deficits in chronic schizophrenia and bipolar disorder with psychotic features. Schizophrenia Res 2012;139:253–9.
22. Umbricht D, Schmid L, Koller R, Vollenweider FX, Hell D, Javitt DC. Ketamine-induced deficits in auditory and visual context-dependent processing in healthy volunteers: implications for models of cognitive deficits in schizophrenia. Arch Gen Psychiatry 2000;57:1139–47.
23. Kreitschmann-Andermahr I, Rosburg T, Demme U, Gaser E, Nowak H, Sauer H. Effect of ketamine on the neuromagnetic mismatch field in healthy humans. Brain Res Cogn Brain Res 2001;12:109–16.

24. Umbricht D, Koller R, Vollenweider FX, Schmid L. Mismatch negativity predicts psychotic experiences induced by NMDA receptor antagonist in healthy volunteers. Biol Psychiatry 2002;51:400–6.
25. Heekeren K, Daumann J, Neukirch A, Stock C, Kawohl W, Norra C, et al. Mismatch negativity generation in the human 5HT2A agonist and NMDA antagonist model of psychosis. Psychopharmacol 2008;199:77–88.
26. Neuner I, Rajkumar R, Brambilla CR, Ramkiran S, Ruch A, Orth L, et al. Simultaneous PET-MR-EEG: Technology, challenges and application in clinical neuroscience. IEEE Trans Radiat Plasma Med Sci 2019;3:377–85.
27. Elmenhorst D, Mertens K, Kroll T, Oskamp A, Ermert J, Elmenhorst EM, et al. Circadian variation of metabotropic glutamate receptor 5 availability in the rat brain. J Sleep Res 2016;25:754–61.
28. Herzog H, Langen KJ, Weirich C, Rota Kops E, Kaffanke J, Tellmann L, et al. High resolution BrainPET combined with simultaneous MRI. Nuklearmedizin 2011;50:74–82.
29. Burger C, Deschwanden A, Ametamey S, Johayem A, Mancosu B, Wyss M, et al. Evaluation of a bolus/infusion protocol for 11C-ABP688, a PET tracer for mGluR5. Nucl Med Biol 2010;37:845–51.
30. Akkus F, Terbeck S, Ametamey SM, Rufer M, Treyer V, Burger C, et al. Metabotropic glutamate receptor 5 binding in patients with obsessive-compulsive disorder. Int J Neuropsychopharmacol 2014;17:1915–22.
31. Deschwanden A, Karolewicz B, Feyissa AM, Treyer V, Ametamey SM, Johayem A, et al. Reduced metabotropic glutamate receptor 5 density in major depression determined by [11C]ABP688 PET and postmortem study. Am J Psychiatry 2011;168:727–34.
32. Del Guerra A, Ahmad S, Avram M, Belcari N, Berneking A, Biagi L, et al. TRIMAGE: A dedicated trimodality (PET/MR/EEG) imaging tool for schizophrenia. Eur Psychiatry 2018;50:7–20.
33. Rota Kops E, Herzog H. Template-based attenuation correction of PET in hybrid MR-PET scanners. J Nucl Med 2008;49:162P.
34. Brambilla, Scheins J, Issa A, Tellmann L, Herzog H, Rota Kops E, et al. Bias evaluation and reduction in 3D OP-OSEM reconstruction in dynamic equilibrium PET studies with 11C-labeled for binding potential analysis. PLoS ONE 2021;16:e0245580.
35. Picard Y, Thompson CJ. Motion correction of PET images using multiple acquisition frames. IEEE Trans Med Imaging 1997;16:137–44.
36. Brambilla, Zeusseu O, Scheins J, Kops ER, Tellmann L, Shah NJ, et al. Annual Congress of the European Association of Nuclear Medicine October 12–16, 2019 Barcelona, Spain. Eur J Nucl Med Mol Imaging 2019;46:1–952.
37. Scheins J, Brambilla CR, Mauler J, Rota Kops E, Tellmann L, Lerche CW, et al. Image-based Motion Correction for the Siemens Hybrid MR/BrainPET Scanner. 57 Jahrestagung der Deutschen Gesellschaft für Nuklearmedizin 2019; Bremen, Germany 2019.
38. Hammers A, Allom R, Koepp MJ, Free SL, Myers R, Lemieux L, et al. Three-dimensional maximum probability atlas of the human brain, with particular reference to the temporal lobe. Hum Brain Mapp 2003;19:224–47.
39. Shirer WR, Ryali S, Rykhlevskaia E, Menon V, Greicius MD. Decoding subject-driven cognitive states with whole-brain connectivity patterns. Cereb Cortex 2012;22:158–65.
40. Smart K, Cox SML, Nagano-Saito A, Rosa-Neto P, Leyton M, Benkelfat C. Test-retest variability of [11C]ABP688 estimates of metabotropic glutamate receptor subtype 5 availability in humans. Synapse. 2018;72:e22041.
41. DeLorenzo C, Gallezot JD, Gardus J, Yang J, Planeta B, Nabulsi N, et al. In vivo variation in same-day estimates of metabotropic glutamate receptor subtype 5 binding using [11C]ABP688 and [18F]FPEB. J Cereb Blood Flow Metab 2017;37:2716–27.
42. Delorme A, Makeig S. EEGLAB: an open source toolbox for analysis of single-trial EEG dynamics including independent component analysis. J Neurosci Methods 2004;134:9–21.
43. Niazy RK, Beckmann CF, Iannetti GD, Brady JM, Smith SM. Removal of FMRI environment artifacts from EEG data using optimal basis sets. NeuroImage 2005;28:720–37.
44. Mullen TR, Kothe CAE, Chi YM, Ojeda A, Kerth T, Makeig S, et al. Real-Time neuroimaging and cognitive monitoring using wearable dry EEG. IEEE Trans bio-Med Eng 2015;62:2553–67.
45. Marino M, Liu Q, Koudelka V, Porcaro C, Hlinka J, Wenderoth N, et al. Adaptive optimal basis set for BCG artifact removal in simultaneous EEG-fMRI. Sci Rep. 2018;8:8902.
46. Gomez-Herrero G, Clercq WD, Anwar H, Kara O, Egiazarian K, Huffel SV, et al. editors. Automatic Removal of Ocular Artifacts in the EEG without an EOG Reference Channel. Proceedings of the 7th Nordic Signal Processing Symposium - NORSIG 2006; 2006 7-92006.
47. Bell AJ, Sejnowski TJ. An information-maximization approach to blind separation and blind deconvolution. Neural Comput 1995;7:1129–59.
48. Winkler I, Haufe S, Tangermann M. Automatic classification of artifactual ICA-components for artifact removal in EEG signals. Behav Brain Funct 2011;7:30.
49. Cousineau D. Representing error bars in within-subject designs in typical software packages. The Quantitative Methods for. Psychology 2014;10:12.
50. Holmes SE, Gallezot J-D, Davis MT, DellaGioia N, Matuskey D, Nabulsi N, et al. Measuring the effects of ketamine on mGluR5 using [^{18}F]FPEB and PET. J Cereb Blood Flow Metab 2019;0:0271678X19886316.
51. Moghaddam B, Adams B, Verma A, Daly D. Activation of glutamatergic neurotransmission by ketamine: a novel step in the pathway from NMDA receptor blockade to dopaminergic and cognitive disruptions associated with the prefrontal cortex. J Neurosci 1997;17:2921–7.
52. Chowdhury GM, Behar KL, Cho W, Thomas MA, Rothman DL, Sanacora G. 1H-[13C]-nuclear magnetic resonance spectroscopy measures of ketamine's effect on amino acid neurotransmitter metabolism. Biol Psychiatry 2012;71:1022–5.
53. Fitzgerald K, Todd J. Making Sense of Mismatch Negativity. Front Psychiatry. 2020;11:468.
54. Escera C, Alho K, Schröger E, Winkler I. Involuntary attention and distractibility as evaluated with event-related brain potentials. Audio Neurootol 2000;5:151–66.
55. Lakatos P, O'Connell MN, Barczak A, McGinnis T, Neymotin S, Schroeder CE, et al. The thalamocortical circuit of auditory mismatch negativity. Biol Psychiatry 2020;87:770–80.
56. Cacciaglia R, Escera C, Slabu L, Grimm S, Sanjuán A, Ventura-Campos N, et al. Involvement of the human midbrain and thalamus in auditory deviance detection. Neuropsychologia 2015;68:51–8.
57. Jin Y, Yang H, Zhang F, Wang J, Liu H, Yang X, et al. The medial thalamus plays an important role in the cognitive and emotional modulation of orofacial pain: a functional magnetic resonance imaging-based study. Front Neurol 2020;11:589125.
58. Hwang K, Bertolero MA, Liu WB, D'Esposito M. The human thalamus is an integrative hub for functional brain networks. J Neurosci 2017;37:5594–607.
59. Bartlett EL. The organization and physiology of the auditory thalamus and its role in processing acoustic features important for speech perception. Brain Lang 2013;126:29–48.
60. Gaebler AJ, Mathiak K, Koten JW Jr., Konig AA, Koush Y, Weyer D, et al. Auditory mismatch impairments are characterized by core neural dysfunctions in schizophrenia. Brain 2015;138:1410–23.
61. Buckner RL, Andrews-Hanna JR, Schacter DL. The brain's default network: anatomy, function, and relevance to disease. Ann N Y Acad Sci 2008;1124:1–38.
62. Hahn B, Ross TJ, Stein EA. Cingulate activation increases dynamically with response speed under stimulus unpredictability. Cereb Cortex 2007;17:1664–71.
63. Deng Z, Wu J, Gao J, Hu Y, Zhang Y, Wang Y, et al. Segregated precuneus network and default mode network in naturalistic imaging. Brain Struct Funct 2019;224:3133–44.
64. Cunningham SI, Tomasi D, Volkow ND. Structural and functional connectivity of the precuneus and thalamus to the default mode network. Hum Brain Mapp 2017;38:938–56.
65. van den Heuvel MP, Mandl RC, Kahn RS, Hulshoff, Pol HE. Functionally linked resting-state networks reflect the underlying structural connectivity architecture of the human brain. Hum Brain Mapp 2009;30:3127–41.
66. van den Heuvel MP, Sporns O. Network hubs in the human brain. Trends Cogn Sci 2013;17:683–96.
67. Gur RC, Turetsky BI, Loughead J, Waxman J, Snyder W, Ragland JD, et al. Hemodynamic responses in neural circuitries for detection of visual target and novelty: An event-related fMRI study. Hum Brain Mapp 2007;28:263–74.
68. Harms L, Parras GG, Michie PT, Malmierca MS. The role of glutamate neurotransmission in mismatch negativity (MMN), a measure of auditory synaptic plasticity and change-detection. Neuroscience 2021;456:106–13.
69. Kompus K, Westerhausen R, Craven AR, Kreegipuu K, Poldver N, Passow S, et al. Resting-state glutamatergic neurotransmission is related to the peak latency of the auditory mismatch negativity (MMN) for duration deviants: An 1H-MRS-EEG study. Psychophysiology 2015;52:1131–9.
70. Stone JM, Bramon E, Pauls A, Sumich A, McGuire PK. Thalamic neurochemical abnormalities in individuals with prodromal symptoms of schizophrenia - relationship to auditory event-related potentials. Psychiatry Res 2010;183:174–6.
71. Hwang K, Bertolero MA, Liu WB, Esposito M. The human thalamus is an integrative hub for functional brain networks. J Neurosci 2017;37:5594.
72. Jones EG. The Thalamus: Plenum Press; 1985.
73. Halassa MM, Acsády L. Thalamic Inhibition: Diverse Sources, Diverse Scales. Trends Neurosci 2016;39:680–93.
74. Pressler RT, Regehr WG. Metabotropic glutamate receptors drive global persistent inhibition in the visual thalamus. J Neurosci 2013;33:2494–506.
75. Cheng C-H, Wang P-N, Hsu W-Y, Lin Y-Y. Inadequate inhibition of redundant auditory inputs in Alzheimer's disease: An MEG study. Biol Psychol 2012;89:365–73.
76. Ji L-L, Zhang Y-Y, Zhang L, He B, Lu G-H. Mismatch negativity latency as a biomarker of amnestic mild cognitive impairment in Chinese rural elders. Front Aging Neurosci. 2015;7:22.
77. Umbricht D, Krljes S. Mismatch negativity in schizophrenia: a meta-analysis. Schizophr Res 2005;76:1–23.

78. Näätänen R. Attention and brain function. Hillsdale: Lawrence Erlbaum Associates, Inc. 1992.
79. Näätänen R, Schröger E, Karakas S, Tervaniemi M, Paavilainen P. Development of a memory trace for a complex sound in the human brain. Neuroreport 1993;4:503–6.

ACKNOWLEDGEMENTS

This work was in part supported by the EU-FP7 funded project TRIMAGE (Nr. 602621). The corresponding author thanks DAAD for financial support (Nr. 57299294). The authors thank Magdalene Vögeling, Silke Frensch, and Suzanne Schaden for their technical assistance. We would also like to thank Shivakumar Viswanathan and Claudia Schmidt for the valuable discussions about analysis and within-subject correction methods. Finally, the authors would like to thank Claire Rick for proofreading the manuscript.

AUTHOR CONTRIBUTIONS

CB: PET bolus-infusion protocol optimization, data acquisition, PET imaging and plasma data analysis, image processing (BP_{ND}), statistical design and analysis, manuscript writing, correction and revision. *TV:* BP_{ND} and EEG correlation analysis, EEG result contributions, and correction and revision. *RR:* data acquisition, EEG data processing, and revision of the manuscript. *JM:* PET bolus-infusion study design, data acquisition, and revision of the manuscript. *AM:* bolus-infusion study design, data acquisition, metabolite-correction design, and setup. *AR:* volunteer screening and revision of the paper. *LO:* volunteer screening and data acquisition. *SR:* data acquisition and revision of the manuscript. *HS:* data acquisition, metabolite correction, and revision of the manuscript. *NK:* data acquisition, metabolite correction, and revision of the manuscript. *NYK:* inputs on interpretation of the biological processes behind BP_{ND} changes. *CW:* study design and revision of the manuscript. *KH:* study design and revision of the manuscript. *WK:* study design and revision of the manuscript. *ERK:* MR-PET attenuation correction, revision, and correction of the manuscript. *LT:* MR-PET hardware and data acquisition. *JS:* PET reconstruction and head-motion correction methodology. *FB:* MR-PET hardware integration and study design. *BN:* revision of the manuscript. *JE:* revision and corrections of the manuscript. *ML*: radiotracer production and quality control. *SS*: radiotracer production and quality control. *HH:* PET study-design discussions, revision, and corrections of the manuscript. *KJL:* revision of the manuscript. *NJS:* MR-PET hardware and revision of the manuscript. *CL:* study design and setup, data-analysis revision, manuscript corrections, and revision. *IR:* study design and setup, approval ethics and BfS, and revision of the manuscript.

COMPETING INTERESTS

These data are part of the Dr. rer. medic thesis at the Medical Faculty of the RWTH Aachen University, Germany of Cláudia Régio Brambilla. There is no potential conflict of interest relevant to this article.

ADDITIONAL INFORMATION

Correspondence and requests for materials should be addressed to Cláudia Régio Brambilla.

Reprints and permission information is available at http://www.nature.com/reprints

Publisher's note Springer Nature remains neutral with regard to jurisdictional claims in published maps and institutional affiliations.

Open Access This article is licensed under a Creative Commons Attribution 4.0 International License, which permits use, sharing, adaptation, distribution and reproduction in any medium or format, as long as you give appropriate credit to the original author(s) and the source, provide a link to the Creative Commons license, and indicate if changes were made. The images or other third party material in this article are included in the article's Creative Commons license, unless indicated otherwise in a credit line to the material. If material is not included in the article's Creative Commons license and your intended use is not permitted by statutory regulation or exceeds the permitted use, you will need to obtain permission directly from the copyright holder. To view a copy of this license, visit http://creativecommons.org/licenses/by/4.0/.

© The Author(s) 2021